RAA 2021 Vol. **21** No. **1**, 11(14pp) doi: 10.1088/1674-4527/21/1/11

http://www.raa-journal.org *http://iopscience.iop.org/raa*

Research in Astronomy and Astrophysics

Computation of the atmosphere-less light intensity curve during a total solar eclipse by using Lunar Reconnaissance Orbiter topography data and the DE430 astronomical ephemeris

Yun-Bo Wang[1], Jian-Guo Yan[1], Mao Ye[1,3], Yong-Zhang Yang[1], Fei Li[1] and Jean-Pierre Barriot[2,1]

[1] State Key Laboratory of Information Engineering in Surveying, Mapping and Remote Sensing, Wuhan University, Wuhan 430079, China; *jgyan@whu.edu.cn, yang.yongzhang@whu.edu.cn*
[2] Geodesy Observatory of Tahiti, University of French Polynesia, BP 6570, 98702 Faaa, Tahiti, French Polynesia
[3] Key Laboratory of Lunar and Deep Space Exploration, National Astronomical Observatories, Chinese Academy of Sciences, Beijing 100101, China

Received 2020 August 30; accepted 2020 October 27

Abstract Observations of the sky irradiation intensity in the visible wavelengths during a solar eclipse permit to model the Sun diameter, a key number to constrain the internal structure of our star. In this paper, we present an algorithm that takes advantage of the precise Moon topography from Lunar Reconnaissance Orbiter to compute, with a high resolution in time, the geometrical part (i.e. top-of-atmosphere, and for a given wavelength) of the sky irradiation at any given location on the Earth during these events. The algorithm is also able to model the Baily's beads. We give as an application the theoretical computation of the light curve corresponding to the solar eclipse observed at Lakeland (Queensland, North Australia) on 2012 November 13. The application to real data, with the introduction of atmospheric and instrumental passbands, will be considered in a forthcoming paper.

Key words: eclipse — Moon — Sun: fundamental parameters

1 INTRODUCTION

The solar diameter is a fundamental parameter in solar physics, used to constrain the internal structure of the Sun. We refer to Rozelot et al. (2018a) and Sofia et al. (2013) for the relation between solar diameter, solar luminosity and climate evolution. Due to the fact that the Sun does not have a solid surface, a precise definition of solar diameter must be agreed upon. We will discuss the modern exact meaning later on. Many different methods and instruments have been used to determine the solar diameter; including meridian circles, Mercury transits, astrolabes, solar diameter monitors, reflecting heliometers and the solar eclipses (Thuillier et al. 2005; Rozelot et al. 2016; Rozelot et al. 2018a). The Greek astronomer Samos (310 BC — 230 BC) is the earliest astronomer known to have measured the solar diameter by analyzing lunar eclipse observations. He assumed a given diameter for the Earth and determined the solar radius as 900 arcsec (Thuillier et al. 2005; Rozelot 2006; Rozelot & Damiani 2012).

The history of measuring solar diameter during solar eclipse dates back to the 18th century. The first observation of a solar eclipse to compute the solar diameter was conducted in 1715 (Fiala et al. 1994), and a summary of measurements of the solar diameter during solar eclipses, from 1715 to 2010, was written by Adassuriya et al. (2011). In 1836, the Baily's beads phenomenon, occurring in total and annular eclipses of the Sun was first recorded in writing (Baily 1836). Baily's beads are caused by the lunar mountains' deep valleys, and craters at the edge of the Moon that break up sunlight (Sigismondi et al. 2012). Before Watts published the Watts' limb charts in 1963 (Watts 1963), the measurement of the solar diameter by solar eclipse observation was considered impossible because the effect of the lunar rugged limb was not known well enough. From 1966 to 2010, Watts' limb charts were widely used in solar eclipse and solar diameter measurement research. However, the lunar limb profiles obtained from the Watts' limb charts sometimes have large errors (Soma & Kato 2002). These errors influence the accuracies of solar diameter measurements; thus, a high-resolution lunar topography data set is needed. In 2009, a global lunar digital elevation model (DEM) data set with a resolution down to 1/16 degree was produced by using the data from the Japanese lunar exploration mission SELENE (Araki et al. 2009). This model was used by Adassuriya et al. (2011), Sigismondi et al. (2012) and Raponi et al. (2012) to determine the solar radius from Baily's beads timing observations. Five years later, the Lunar Reconnaissance Orbiter (LRO) mission from NASA published a higher resolution 1/256 degree DEM data in 2014. These DEM data are the most accurate lunar topography data at the time of the writing of these lines.

It is now time to precise what we mean by "solar diameter". First, this notion implies that the Sun can be considered as a pure sphere. Our Sun is rotating with a rotation period of 24.47 days at the equator and almost 38 days at the poles. It is argued that there is a 10 km difference between the polar and equatorial diameter (Rozelot & Damiani 2011; Kuhn et al. 2012; Meftah et al. 2016). No gravity flattening is observed from the tracking of Deep Space probes (an upper limit of 2×10^{-7} was given by Fienga et al. (2011). Within an accuracy of $+/-$ 10 km, it is therefore justified to use only one parameter to characterize the Sun "size" (Meftah et al. 2016). Secondly, the Sun limb is not a solid surface, and show a progressive darkening, of wavelength-dependent character, at its telescopic limit (Hestroffer & Magnan 1998). The most common modern definition is to use a wavelength-based approach, such as Lamy et al. (2015) and Rozelot et al. (2016), where the solar diameter is defined as the value observed at 540 nm optical wavelength (green light). To observe the light-curve at one wavelength implies the use of narrow-band filters, reducing the amount of light received by photometers, and so decreases the signal-to-noise ratio. To observe over a wider range of wavelength improves this ratio, but then a suitable average of "wavelength-dependent solar diameters" must be defined (Rozelot et al. 2016). In 2018, the solar radius determinations made during the 2012 Venus transit by the Solar Diameter Imager and Surface Mapper (SODISM) telescope onboard the PICARD spacecraft were published. At 535.7 nm, the solar radius was found equal to $696\,134 \pm 261$ km, against $696\,156 \pm 145$ km at 607.1 nm and $696\,192 \pm 247$ km at 782.2 nm. It indicates that the solar radius wavelength dependence on the visible and the near-infrared wavelength is extremely weak (Meftah et al. 2018). In 2015, Resolution B3 of the International Astronomical Union defined a new value of the nominal wavelength-independent solar radius (695 700 km) that was different from the canonical value used until then (695 990 km) (Prša et al. 2016). This nominal solar radius corresponds to the solar photospheric radius suggested by Haberreiter et al. (2008) who resolved the long-standing discrepancy between the seismic and photospheric solar radii (Mamajek et al. 2015). We will use this new value (695,700 km) in all the computations done in this paper.

In this work, we used the LRO lunar DEM data set to calculate with high accuracy the atmosphere-less light curve for the solar eclipse observed at Lakeland, Queensland ($15°51'30''$S, $144°51'20''$E) on 2012 November 13. By atmosphere-less, we mean that we did not consider the extinction of solar light caused by atmosphere gases and aerosols, the scattering of the Sun light by the atmosphere, as well as photometer passbands. We used a pure geometrical optics approach (i.e. an "infinite" frequency monochromatic approximation for light), taking into account the light-time between Moon and Earth.

2 DATA AND METHOD

2.1 LRO Digital Elevation Model Data

Between July 2009 and July 2013, the Lunar Orbiter Laser Altimeter (LOLA; Smith et al. 2010), an altimeter instrument onboard the LRO spacecraft (Tooley et al. 2010) gathered more than 6.5 billion laser altimetric measurements along ground tracks separated by 1.25 km at the Moon equator with a separation of about 57 m along-track between laser shots. The diameter of the cross-like laser shot imprint on the Moon surface was about 50 m for an LRO nominal polar orbit of 50 km altitude. The crossovers between the altimetric tracks on the Moon surface were used by the LOLA team to reduce the orbital error of LRO down to a few tens of centimeters. The average accuracy of each laser shot point after crossover corrections is estimated to be better than 20 meters in horizontal position and around 1 meter in Moon radius (Mazarico et al. 2012).Thereafter, the calibrated altimetric measurements were gridded (Digital Elevation Model) with the algorithm of Wessel et al. (2013) with a resolution of 256 pixels per degree in selenographic latitude and longitude, corresponding to 118 m on the Moon equator (Neumann et al. 2011). Gaps between tracks, up to 4 km at the equator, were filled by interpolation (Smith et al. 2010). We downloaded these grid values (file "Lunar_LRO_LOLA_Global_LDEM_118m" from the LRO website (see Acknowledgements section). The grid values were computed by subtracting the lunar reference radius of 1737.4 km from the surface radius measurements (Archinal et al. 2011). An improved digital terrain model, limited to latitudes $+/-$ 60 degrees, exists (Barker et al. 2016) but cannot be used for this work because we need the limb from pole to pole.

The latest DE430 ephemeris (Williams et al. 2013; Folkner et al. 2014) from the Jet Propulsion Laboratory, embedded in the SPICE kernel library (*https://naif.jpl.nasa.gov/naif/toolkit.html*, version N0066 in our case) was employed to generate the positions and velocities of the Earth and the Moon. It is valid from 1549 December 21 to 2650 January 25. According to Urban & Kenneth Seidelmann (2013) and W.M. Folkner (personal communication, 2020 July 7), the DE430 ephemeris uncertainty in the relative position between the Earth and the Moon is around 1 meter.

2.2 Observation Model

2.2.1 *Limb geometrical model*

The lunar limb is defined as the lines emanating from the observer that are tangent to the Moon. The lunar limb is in the "plane of sky", a plane perpendicular to the direction of the observer to the center of the Moon. The observational geometry is given in Figure 1.

As shown in Figure 1, MF and MG are the limb points as seen by the observer, defining a circle in three dimensions. MF can be computed by:

$$\overrightarrow{MF} = \overrightarrow{OF} - \overrightarrow{OM} \tag{1}$$

OM is the vector of observer to the center of the Moon. OF is:

$$\overrightarrow{OF} = D\boldsymbol{\mu} + r(\cos\theta \boldsymbol{i} + \sin\theta \boldsymbol{j}) \tag{2}$$

where $\boldsymbol{\mu}$ is the unit vector of $\overrightarrow{OM}$, $\boldsymbol{i}$ and $\boldsymbol{j}$ are two orthogonal directions in the plane of sky. $\boldsymbol{i}$ and $\boldsymbol{j}$ can be computed by:

$$\boldsymbol{i} = \boldsymbol{\mu} \times \boldsymbol{z} \qquad \boldsymbol{j} = \boldsymbol{\mu} \times \boldsymbol{i} \tag{3}$$

where $\boldsymbol{z}$ is the local zenith of the observer. All these vectors are functions of time. D is the distance between the observer and the plane of sky and r is the radius of the limb profile. D and r are defined by:

$$D = d\left(1 - \left(\frac{R}{d}\right)^2\right) \qquad r = R\sqrt{1 - \left(\frac{R^2}{d}\right)} \tag{4}$$

where d is the distance between the observer and the center of the Moon.

To simplify the problem, a basic assumption could be to assume that the observer is at an infinite distance from the Moon. In this case, we have D=d and r=R, and the limb is a great circle on the Moon surface. We will see in the next chapter that this assumption is not sufficiently accurate. The distances in Equations (1)–(4) have to be understood as "light- time" distances. The light takes slightly more than one second to cross the Moon-Earth distance, therefore, the $\overrightarrow{OM}$ vector is the solution of the equation:

$$c\tau = \|\overrightarrow{O(t)M(c-\tau)}\| \tag{5}$$

where c is the speed of light, t is the time recorded by the observer O, τ is the light-time between the point M and the point O and $\|.\|$ is the Euclidean norm. This equation is solved iteratively by the SPICE library. The change of coordinates between the LRO DEM, given in the Moon mean equator (MME) frame, and the limb frame is also handled by the SPICE library.

Table 1 Eclipse parameters for the Lakeland (North Australia) eclipse on 2012 November 13. The eclipse magnitude (*) in the table is the fraction of the Sun's diameter obscured by the Moon. The mean radius of the Moon is assumed to be nominally 1737.4 km and the radius of Sun is nominally fixed at 695 700 km (IAU resolution 2015-B3). The coordinates of the Sun and the Moon were computed from the DE430 ephemeris. The geographical coordinates of the observer are: $15°51'30''$S, $144°51'20''$E.

Calender Date	2012-NOV-13
First Contact (Eclipse Start)	19:44:05 (UTC)
Second Contact (Totality begins)	20:37:38 (UTC)
Mid-Totality Time	20:38:24 (UTC)
Third Contact (Totality ends)	20:39:12 (UTC)
Fourth Contact (Eclipse ends)	21:38:35 (UTC)
Eclipse Magnitude*	1.0375
Duration of Totality	1 min 34 s

2.2.2 *Example of limb computation*

We now illustrate the computation of the Moon limb by using Equations (1)-(5), in the case of the solar eclipse observed on Lakeland on 2012 November 13 (see Table 1 for details).

Figure 2 shows the Moon limb, as seen from the observer in Lakeland, plotted on the Moon surface at mid-totality.

The limb profiles for both the finite-distance and infinite-distance observers are shown in Figure 3, enlarged by a factor of 40 for legibility.

Figure 4 shows clearly that the infinite-distance approximation is too crude. The time for the right border of the Moon to cross the Sun surface, as seen from the observer at Lakeland, is 3213 seconds (First to Second contacts, see Table 1). As the mean diameter of the Moon is 3474.8 km, this means that the velocity of the Moon in the plane-of-sky of the observer is around 1.08 km s^{-1}, therefore a distance of 770 m is equivalent to 0.713 s

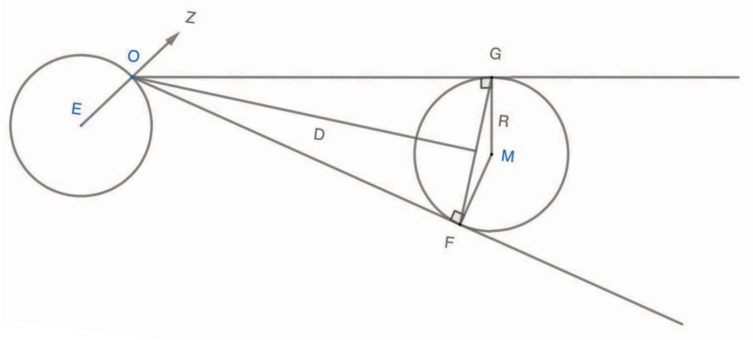

Fig. 1 Finite-distance observer model. E is the center of the Earth, O is the observer on the Earth surface and M is the center of the Moon. The Z direction is the local zenith of the observer. G and F are the limb points as seen from the observer.

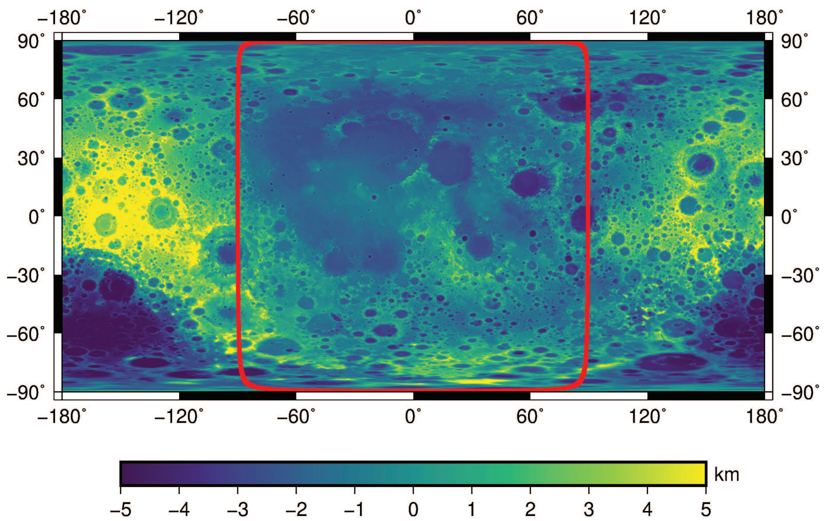

Fig. 2 The Moons limb plotted in the Moon surface, (*red line*) at 2012-NOV-13 20:38:24 UTC, as observed from Lakeland on 2012 November 13. The two cases for limb computations (finite -distance and infinite-distance observers) cannot be distinguished in this figure. The base map is the topographic map from the LRO mission.

in the timing of the Baily's beads, a totally unacceptable value, because the timing accuracy for the measurements is typically at the level of 1 millisecond.

From a theoretical point-of-view the limb must be recomputed at each observation time, both for the timing of the Baily's beads and for light curves, as the Moon rolls back and forth around the sub-Earth point as the result of astronomical forcing (librations, see Rambaux et al. 2010). But this comes with a heavy price-tag in terms of CPU time. Hopefully, this burden can be reduced to a manageable level by considering the resolution of the Moon DEM and the fact that only the daily libration amplitude, a small daily oscillation due to Earth's rotation, which carries the observer on Earth first to one side and then to the other side of the straight line joining Earth's and Moon's centers, is the only one of interests for us. Its amplitude is less than one degree (Yang et al. 2017) in the plane-of-sky. This means about 0.1 degree for two hours, the duration of the Lakeland eclipse from the first to the fourth contacts. As the resolution of the Moon DEM is 1/256 degree, i.e. 108 m at Moon equator, this means that during the two hours eclipse, the limb is displaced by 25 pixels on the Moon surface (0.1 / (1./.256)). This also means that the limb should be recalculated only every 2h / 0.1×(1. / 256.) that is to say around 4 min 30 s. This corresponds to a one pixel displacement caused by the diurnal libration for the DEM. As the timing of the Baily's beads is done during the second and third contacts, only separated by 1 min 34 s for the Lakeland example, this means that we can assume that the limb computation can be performed only once for this timing. For the whole eclipse, we only need to recompute the limb about 25 times. Our software permits the recomputation of the limb with any time resolution. The maximum of the differences around totality between a light curve computed with the

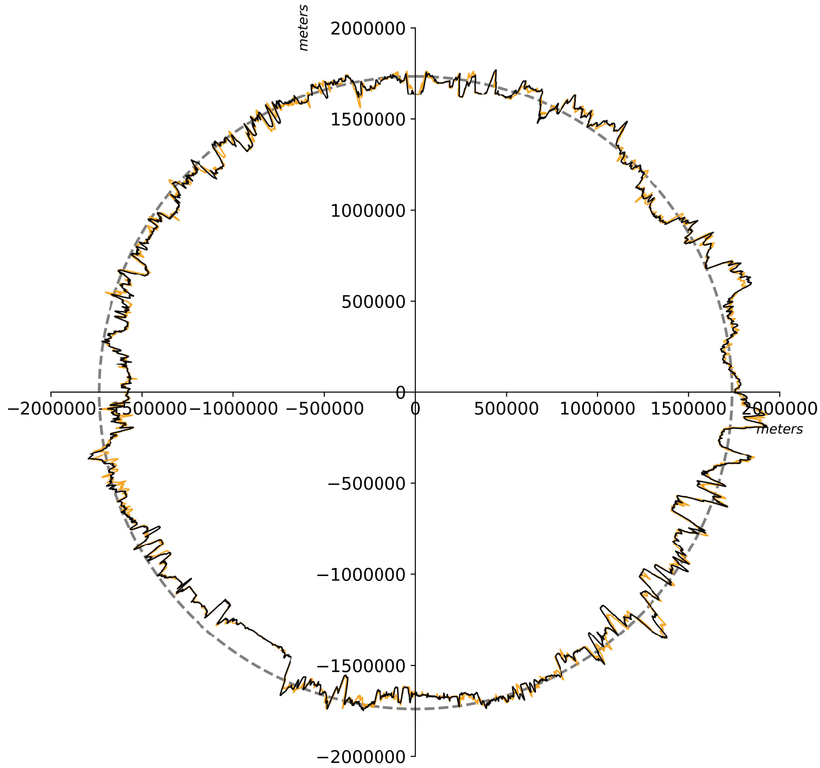

Fig. 3 Comparison between the lunar limb as observed from the Earth at a finite distance (*orange curve*) and the lunar limb (*black curve*) observed from an infinite distance along the same line-of-sight. This figure corresponds to the case of the solar eclipse observed at Lakeland (North Australia) on 2012 November 13. The origin of polar coordinates is dictated by the local zenith of the observer at the time of the observation (2012-NOV-13 20:38:24 UTC, see Eqs. (1)-(5)).

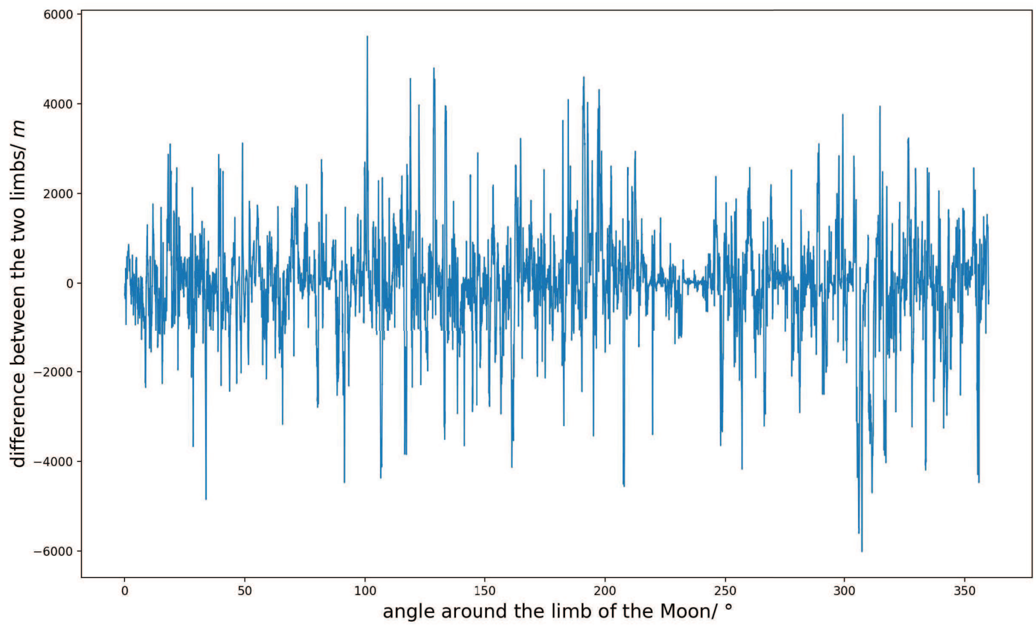

Fig. 4 Differences between the two lunar profiles plotted in Fig. 3 (finite-distance versus infinite-distance observers). The average of differences is 770.17 m, the maximum of differences is 6018 m and the standard deviation is 1165.25 m. The time sampling is 1 s.

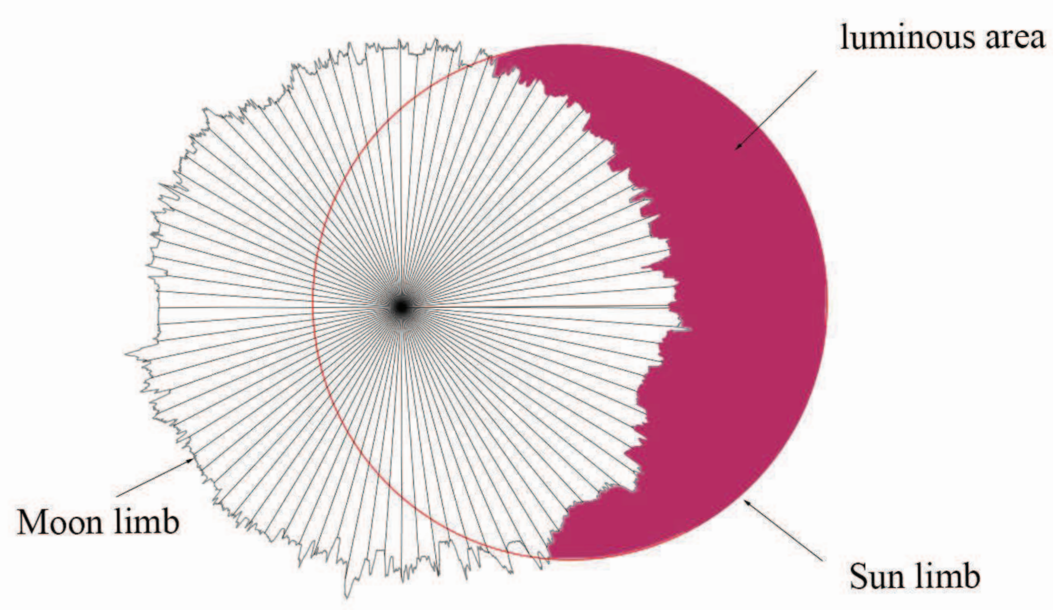

Fig. 5 Luminous area at 20:20:24 2012-Nov-13. The red area circle is the plane-of-sky illuminated part of the Solar disk as seen by an observer at Lakeland, the black curve is the Moon limb. UTC time is 20:20:24 2012-Nov-13. The solar radius is fixed at 695 700 km (Table 1).

limb computed once and the limb computed at each time sampling is 2.69×10^{-6} (Fig. 7(d)).

2.3 Computation of Light Curves

In this section, we compute the geometrical optics approximation of the Sun illumination on Earth surface during an eclipse. To obtain the light intensity as measured by a photometer on Earth surface, three other parameters are needed: (a) The (frequency-dependent) extinction of light caused by the atmosphere, and especially by its aerosol contents; (b) The instrument (convolution) function of the photometer (filters, photodiode characteristics); (c) The orientation at any time of the photometer boresight with respect to the line-of-sight Observer-Moon. This is not treated in this paper, because they are site and instrument dependents. This raw illumination function is defined as the angular area of the Sun surface not obscured by the Moon. For this purpose, the Moon surface is divided in radial triangles, the external part of the triangles being defined by the Moon limb (see Fig. 5). The problem is then to compute the common area between each of these triangles and the disk of the Sun, and to sum up all the triangle contributions. Because the resolution of the LRO DEM is 118 m, which is equivalent to 1/256 degree, we divided the whole lunar limb in 1/256 degree sub-parts, obtaining 92 160 small triangles.

The mathematics of the computation of the intersection between a disk and a triangle are not difficult, but tedious, so we discuss them in the Appendix.

3 RESULT

3.1 Light Curve

Lamy et al. (2015) demonstrated that the modeling of the light curve, in the neighborhood of the second and third contacts is a powerful way to determine the diameter of the Sun from ground based photometric curves. Their main argument is that, by observing near the second and third contacts, the bulk of the solar disk is occulted, resulting in very low instrumental and atmospheric levels of stray light (scattered light not coming directly from the Sun). Figure 6 exhibits the theoretical modeling of such a light curve over three hours for the Lakeland case.

The difference in illumination caused by the topography of the Moon is at a level of 0.01 % of the total illumination of the unobscured Sun. Figure 6(b) show clearly that the left and right parts of the light curve, before and after the totality, computed from the true limb, are not symmetrical. This happens because the topography of the Moon is highly rugged. The mean radius of the Moon is, as seen from the observer, simply a poor approximation of the limb. A better approximation of the limb, of course only strictly valid for the time of the eclipse, would be the mean radius of the limb, as seen from the observer. It would be even better to consider two “mean” radiuses, the first one corresponding to the half of the Moon limb at play between the first and second contact; and a second one corresponding to the half of the Moon limb at play between the third and fourth contacts (Barriot & Prado 2013). Figure 7(a) shows the light curve from 20:36:00

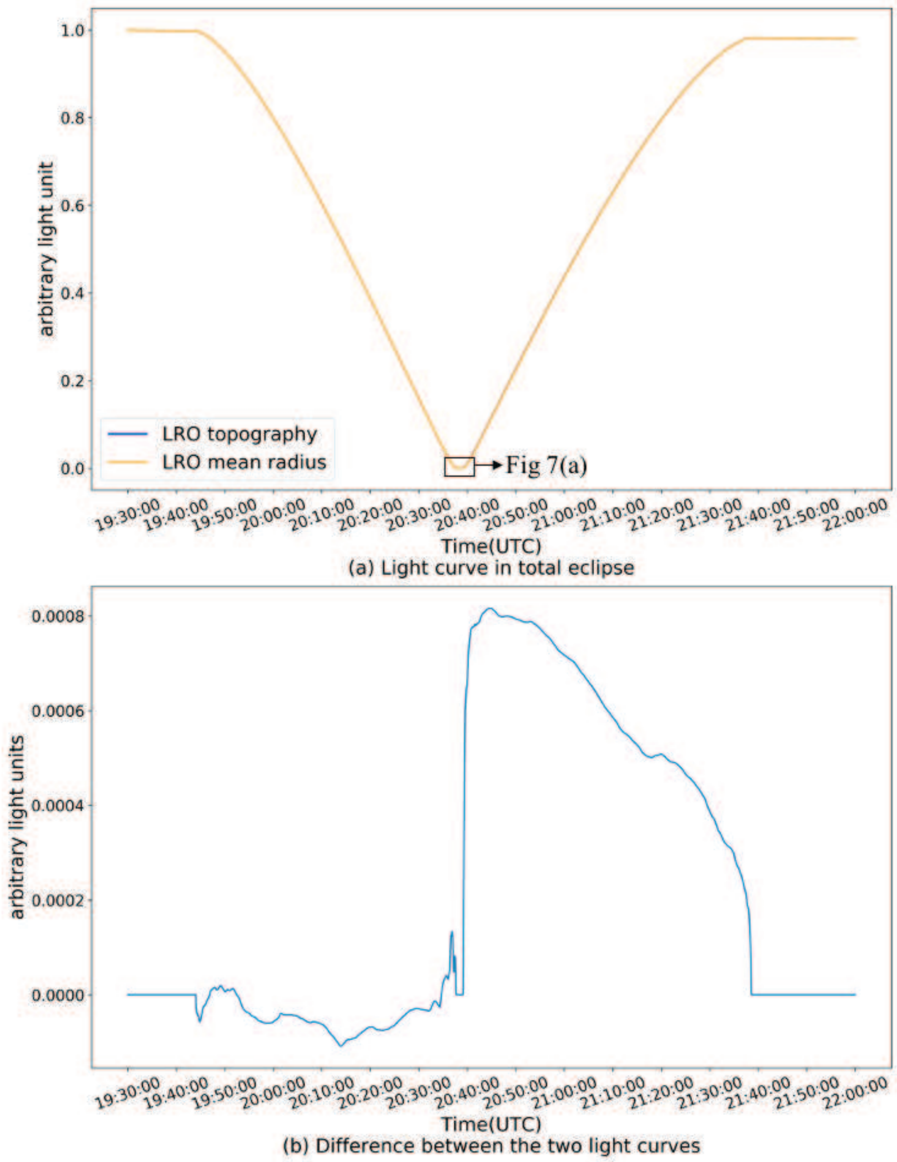

Fig. 6 (a) Theoretical light curves for the Lakeland observer (blue: computation with LRO Moon limb, yellow: computation with the LRO Moon mean radius of 1737.4 km). The radius of the Sun is fixed at 695 700 km (see Table 1) for the whole 2.5 h eclipse duration, from 2013-Nov-13 19:30:00 to 2013-Nov-13 22:00:00. No difference between the two light curves can be seen by eye. See Fig. 7(a) for a zoom of the box area. The two light curves (a) and (b) have been normalized to their maximum values. (b) Differences between the two light curves in the top subfigure 6(a). The time sampling is 1 s.

to 20:41:00 (total eclipse from 20:37:38 to 20:39:12). Before the second contact the best fit is obtained for a limb "radius" of 1736.85 km, and for a limb radius of 1735.55 km after the third contact. This means that the mean topography near the position of third contact is lower than the mean topography near the second contact (see also Fig. 6(b)).

Two error sources show up in the light curve computation. The first one is the error contaminating the DE430 ephemeris, and the second one is the error on the lunar DEM. These errors were already discussed in Section 2.1: the average accuracy of the DEM grid values is around 1 meter (Moon radius) and the DE430 ephemeris uncertainty in the relative position between the Earth and the Moon is also at the level of 1 meter. We estimated (Fig. 8) the error in the nominal light curve by adding small errors (with plus or minus sign, or zero) at these levels in both the nominal DEM and the nominal Earth-Moon distance, and making the relative differences in the corresponding light curves with respect to the nominal

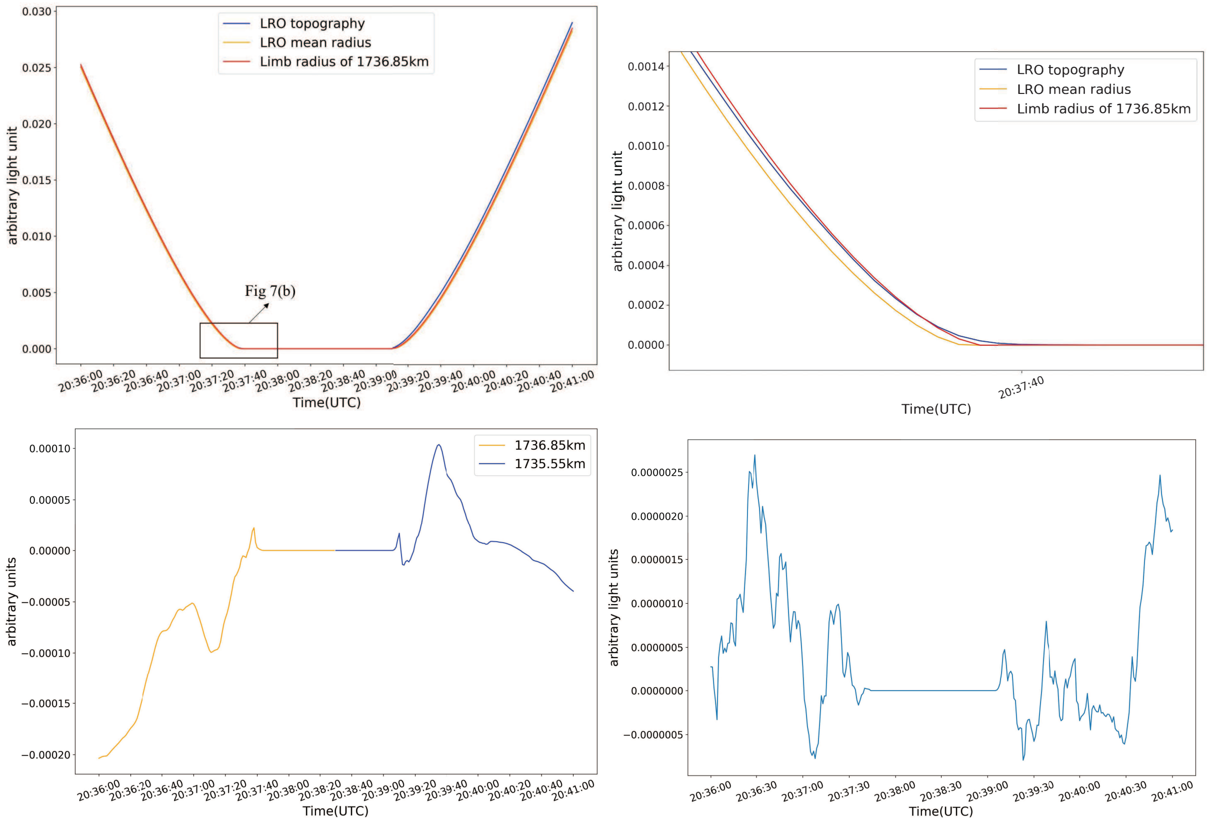

Fig. 7 (a) Light curve "in total eclipse" for a duration of 5 minutes around totality (boxed area in Fig. 6(a)), blue: light-curve computed from the LRO lunar topography, orange: light-curve computed by considering a disk approximation of the Moon limb with a radius of 1737.4 km (LRO value), red: light-curve computed by a disk approximation of the Moon limb with a radius of 1736.85 km corresponding to the mean of the limb topography of 1736.85 km (a good fit for the second contact, but a poor one for the third contact). (b) Zoom at the time of the second contact, (c) Differences between the LRO topography light curve during totality (Fig. 7(a)) and the light curve computed with two limbs mean radiuses: 1736.85 km before the second contact and 1735.55 km after the third contact, (d) Difference between the light curves with the limb computed at each sampling time and the limb only computed once (at mid-totality). The time sampling is 1 s.

light curve. The relative error is dominated, by two orders of magnitude, by the DEM error, and ranges between 10^{-5} and 10^{-3} at the second and third contacts.

The goal of this study is ultimately to show that variations in the solar diameter can be seen in the photometry curve. The expected variations of solar diameter are at a level of 400 milliarseconds, corresponding to 145 km in solar radius (Rozelot et al. 2018b). To test this sensitivity, we perturbed the solar radius by a 10^{-6} variation (695 m), and computed the relative error between the light curve with the perturbed solar radius and the nominal light curve (violet curve in Fig. 8). The relative error caused by the solar radius variation dominates by two orders of magnitude the DEM relative error. As the errors in the Moon LRO DEM and in the DE430 ephemeris are both at a meter-level scale, this means that, at least theoretically, a sensitivity at the level of 100 m in the determination of the solar radius can be achieved by our approach. A conservative number is certainly around a 1 km accuracy.

3.2 Baily's Beads

The Baily's beads, or diamond ring effect, named after Francis Baily, who observed and explained the phenomenon during the 1836 May 15 solar eclipse seen at Inch Bonney in Scotland, occur when beads of sunlight shine through the valleys perpendicular to the Moon limb. The diamond ring effect is when several beads shine as the ring of diamonds of a queen's crown around the lunar silhouette. Figure 9 shows the relative position of the Sun and the Moon at the times of the four contacts as seen from the observer at Lakeland, and Figure 10 is a snapshot of the Baily's beads evolution during the second contact (Fig. 9b). The accuracy of the timing of the Baily's beads is also dominated by the DEM error, and we estimate it to be at the millisecond level (1 m in DEM accuracy divided by the orbital velocity of the Moon (1 km s^{-1}), plus the rotational velocity of the observer on Earth surface (4000 km d^{-1} at the equator).

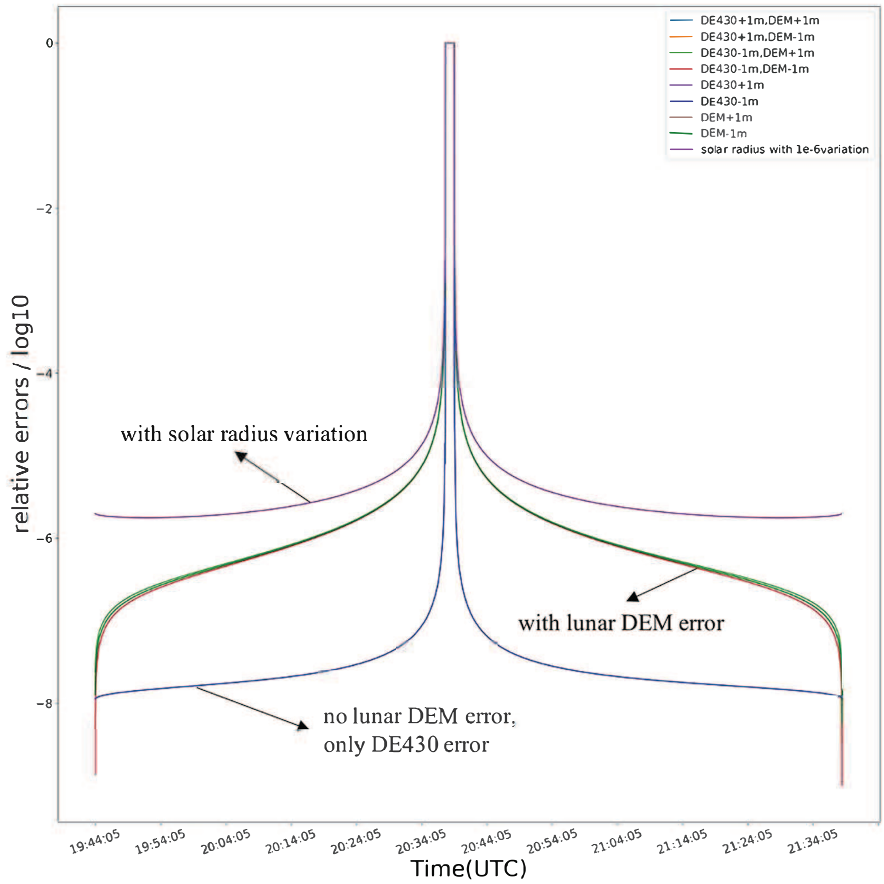

Fig. 8 Estimation of the relative error in the light-curve for the Lakeland observer. The Y axis is the base 10 logarithm of relative errors. The error settings of the eight cases studied are defined in the label: green: six error curves with a lunar DEM error, blue: two error curves with a DE430 ephemeris error only, violet: error curve with 10^{-6} solar radius variation of the nominal 695 700 km Sun radius value (Table 1). The values of Y are set to zero when the relative errors are zero. The relative error is dominated, by two orders of magnitude, by the lunar DEM error with respect to the DE430 ephemeris error. The time sampling is 1 s. The lunar limb was recomputed every 4 min 30 s.

4 CONCLUSIONS

The observation of solar eclipses is certainly one of the best ways to measure the diameter of the Sun, a key parameter in the modeling of the inner dynamics of our star.

In this paper, we focused on the astronomical and astrophysical tools to compute the atmosphere-less part of this computation, by considering the latest DEM model of the Moon from the LRO spacecraft and one of the latest ephemeris of the Earth-Moon system (DE430). Our Python code provides astronomical raw illumination data and timing along the line-of-sight Observer-Center-of-Moon with a millisecond resolution. As an application, we computed an atmosphere-less model of the eclipse observed from Lakeland in North Australia ($15°51'30''$S, $144°51'20''$E) on 2012 November 13. Our study demonstrates that a photometer with a proper calibration of its optoelectronics and good timing resolution, mounted onboard a spacecraft, can detect variations in the solar diameter with an accuracy better than 1 km, and even allow a measurement of solar oblateness. Using photometers on ground is cheaper but more challenging. The limiting factor is ultimately the Earth atmosphere (absorption and scattering). Our next work will deal with the Earth atmosphere effect in real data processing.

Acknowledgements This research was supported by the National Natural Science Foundation of China (U1831132 and 41804025), grant of Hubei Province Natural Science (2018CFA087), also supported by the grant from Key Laboratory of Lunar and Deep Space Exploration, CAS, and LIESMARS Special Research Funding. Planetary ephemerides files can be downloaded from *https://naif.jpl.nasa.gov/pub/naif/JUNO/kernels/spk/*(DE430). LRO DEM data can be downloaded from *https://pds-geosciences.wustl.edu/lro/lro-l-lola-3-rdr-v1/lrolol_1xxx/data/(ldem_256.jp2)*. Jean-

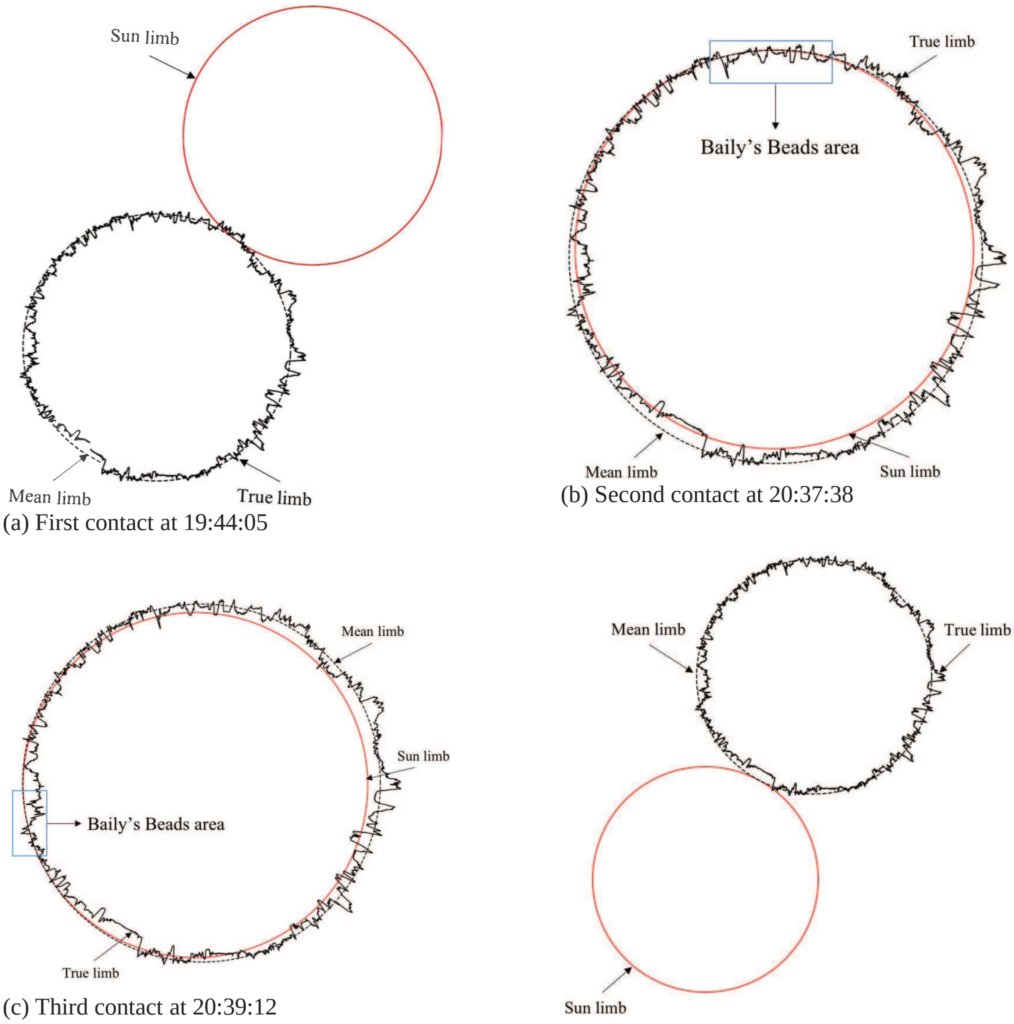

(a) First contact at 19:44:05

(b) Second contact at 20:37:38

(c) Third contact at 20:39:12

(d) Fourth contact at 21:38:35

Fig. 9 The four contacts between the Moon and the Sun during the Lakeland eclipse. The topography of the Moon has been enlarged by a factor of 40 to show details. The contact times are defined at the contacts between the circular mean limb of the Moon and the circular disk of the Sun with a nominal 695 700 km radius (Table 1), not the contacts between the topography of the Moon and the Sun disk. The boxed areas in Fig. 9(b), Fig. 9(c) are the areas of the Moon concerned by the apparition of Baily's beads. Fig. 10(b) shows a zoom of the Baily's beads during the second contact (Fig. 9(b)).

Pierre Barriot was funded through a DAR grant in planetology from the French Space Agency (CNES).

Appendix A: COMPUTATION OF THE COMMON AREA BETWEEN A TRIANGLE AND A DISK

In this section, we explored how to compute the intersection area between a disk and a triangle. Nine cases are listed, as shown in Figure A.1.

We obtain nine different cases:

Case 1: 0 vertices of the triangle in circle, 0 edge intersects the circle (a);

Case 2: 0 vertices of the triangle in circle, 0 edge intersects the circle (b);

Case 3: 0 vertices of the triangle in circle, 1 edge intersects the circle;

Case 4: 0 vertices of the triangle in circle, 2 edges intersect the circle;

Case 5: 0 vertices of the triangle in circle, 3 edges intersect the circle;

Case 6: 1 vertex of the triangle in circle, 0 edge intersects the circle;

Case 7: 1 vertex of the triangle in circle, 1 edge intersects the circle;

Case 8: 2 vertices of the triangle in circle, 0 edge intersects the circle;

Case 9: 3 vertices of the triangle in circle, 0 edge intersects the circle.

We adopted different ways to compute the area of

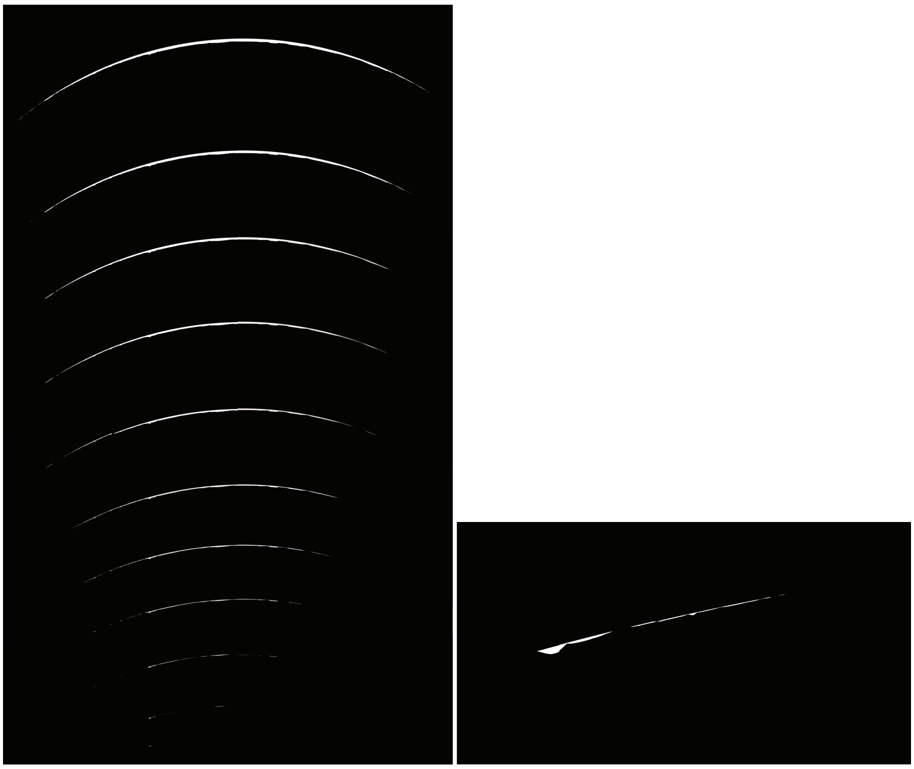

Fig. 10 Baily's beads modeled time evolution as seen by the Lakeland observer. White denotes the visible part of Sun. (a) The simulation of Baily's beads during second contact (from 20:37:18 to 20:37:38, Fig. 9(b)). The time interval between two consecutive pictures is 2 s. (b) The enlargement of the last subplot to show details.

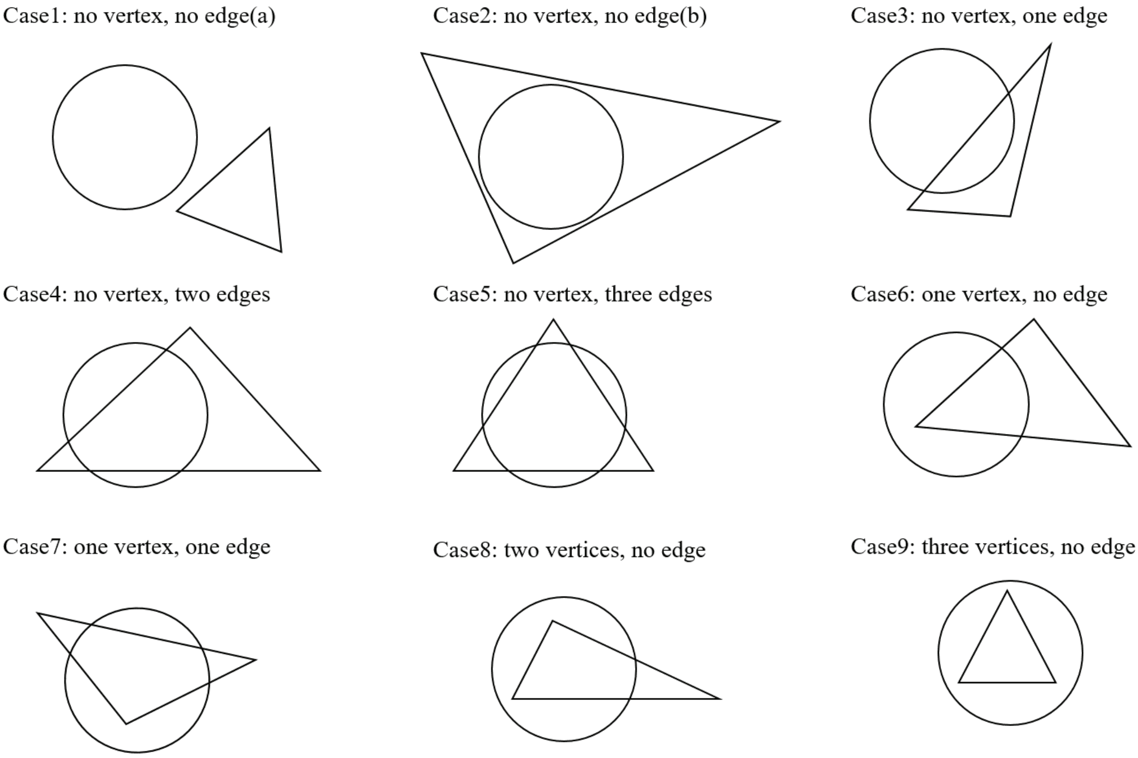

Fig. A.1 The nine cases of intersections between a triangle and a circle (adapted from *https://stackoverflow.com/questions/540014/compute-the-area-of-intersection-between-a-circle-and-a-triangle*).

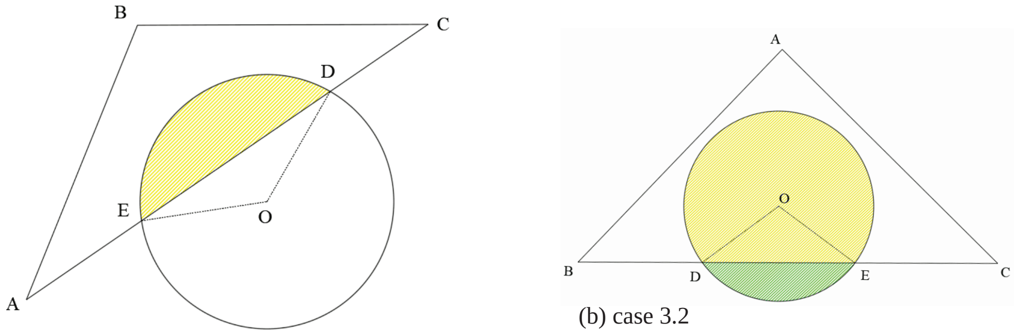

(a) case 3.1

(b) case 3.2

Fig. A.2 The two sub-cases of case 3. (a) case 3.1 the intersection area is the small circular lens, (b) case 3.2 the intersection area is the large circular lens.

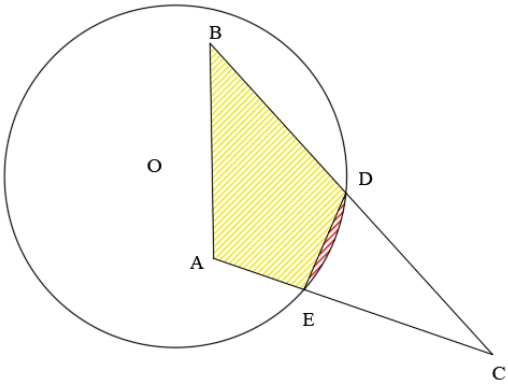

Fig. A.3 Two parts of intersection.

intersection: For case 1: The intersection area equals the surface of the circle:

$$\text{area}_{\text{case1}} = \pi r^2 \tag{A.1}$$

where r is the radius of the circle.
For case 2:

$$\text{area}_{\text{case2}} = 0 \tag{A.2}$$

For case 3: There are two sub-cases, depending whether or not the center of the circle is in the triangle. We plotted these two sub-cases in Figure A.2. In Figure A.2, the area of intersection is shown in yellow.

As shown in Figure A.2(a), the center of the circle is not in the triangle; the area of intersection is the lens shown in yellow, calculated as:

$$\text{area}_{\text{case3.1}} = 1/2\left(\theta r^2 - r\cos\left(\frac{\theta}{2}\right)\right) \tag{A.3}$$

where is:

$$\text{area}_{\text{case3.1}} = 2\arcsin(l/2r) \tag{A.4}$$

and l is the length of the line segment, which intercepts the circle and r is the radius of the circle. As shown in Figure A.2(b), the center of the circle is in the triangle, the area of intersection equals the area of the circle minus the area of the circular lens:

$$\text{area}_{\text{case3.2}} = \pi r^2 - 1/2\left(\theta r^2 - r\cos\left(\frac{\theta}{2}\right)\right) \tag{A.5}$$

where l is the length of the line segment, which intercepts the circle and r is the radius of the circle. We used a common strategy to compute the intersection area in case 4, case 5, case 6, case 7, and case 8. As shown in Figure A.3, the area of intersection can be divided into a polygon and a lens. We computed every partial area and added them up to obtain the area of intersection.

The different ways to divide areas of intersection in cases 4-8 are shown in Figure A.4.

The area of the polygon in cases 4 through 8 is calculated as:

$$\begin{aligned}\text{area}_{\text{polygon}} = \frac{1}{2}[&(x_1y_2 + x_2y_3 + x_3y_4 + \cdots + x_ny_1) \\ &- (y_1x_2 + y_2x_3 + y_3x_4 + \cdots + y_nx_1)]\end{aligned} \tag{A.6}$$

where (x_n, y_n) are the coordinates of the vertices of the polygon. The area of the lens can be calculated by:

$$\text{area}_{\text{circular lens}} = 1/2\left(\theta r^2 - r\cos\left(\frac{\theta}{2}\right)\right) \tag{A.7}$$

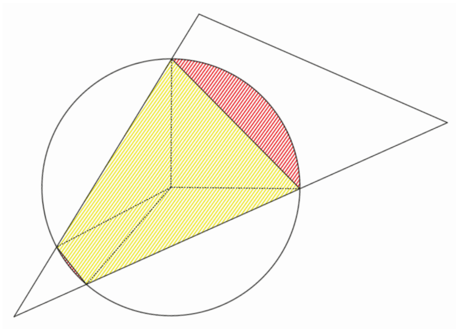

(a) case 4

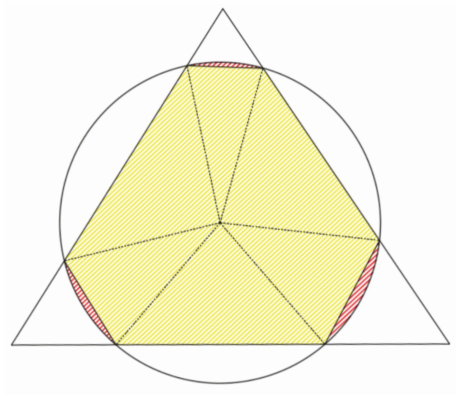

(b) case 5

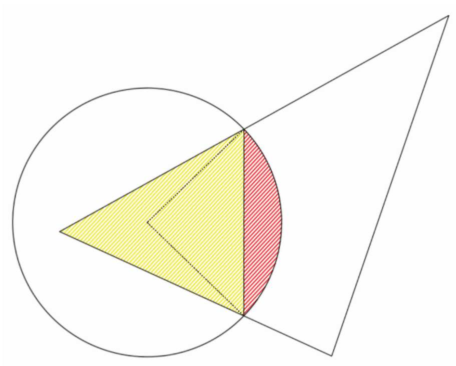

(c) case 6

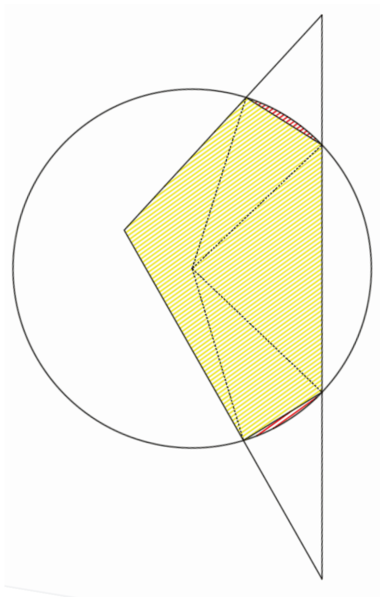

(d) case 7

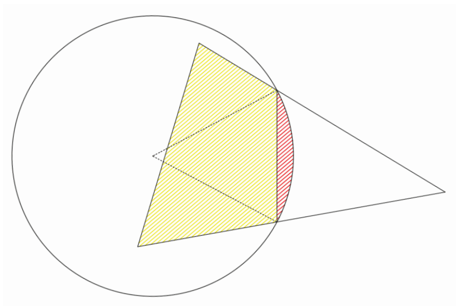

(e) case 8

Fig. A.4 Different ways to divide the intersection area. (a): case 4, (b): case 5, (c): case 6, (d): case 7 and (e): case 8. The yellow part is a polygon, the red part is a circular segment (lens).

So, the area of intersection is

$$\mathrm{area}_{\mathrm{case4,5,6,7,8}} = \mathrm{area}_{\mathrm{polygon}} + \mathrm{area}_{\mathrm{circular\ lens}} \quad (\mathrm{A.8})$$

For the case 9 mentioned in Figure A.1: The area of intersection equals the area of the triangle:

$$\mathrm{area}_{\mathrm{case9}} = \sqrt{s(s-a)(s-b)(s-c)} \quad (\mathrm{A.9})$$

where s is half the perimeter of the triangle:

$$s = 0.5(a + b + c) \quad (\mathrm{A.10})$$

and where a, b, c are the lengths of the edges of the triangle.

References

Adassuriya, J., Gunasekera, S., & Samarasinha, N. 2011, Sun and

Geosphere, 6, 17
Araki, H., Tazawa, S., Noda, H., et al. 2009, Science, 323, 897
Archinal, B. A., A'Hearn, M. F., Bowell, E., et al. 2011, Celestial Mechanics and Dynamical Astronomy, 109, 101
Baily, F. 1836, MNRAS, 4, 15
Barker, M. K., Mazarico, E., Neumann, G. A., et al. 2016, Icarus, 273, 346
Barriot, J. P., & Prado, J. Y. 2013, in PICARD Third Scientific Workshop, 25-26 September 2013, CNES Headquarters, Paris
Fiala, A. D., Dunham, D. W., & Sofia, S. 1994, Sol. Phys., 152, 97
Fienga, A., Laskar, J., Kuchynka, P., et al. 2011, Celestial Mechanics and Dynamical Astronomy, 111, 363
Folkner, W. M., Williams, J. G., Boggs, D. H., Park, R. S., & Kuchynka, P. 2014, Interplanetary Network Progress Report, 42-196, 1
Haberreiter, M., Schmutz, W., & Kosovichev, A. G. 2008, ApJL, 675, L53
Hestroffer, D., & Magnan, C. 1998, A&A, 333, 338
Kuhn, J. R., Bush, R., Emilio, M., & Scholl, I. F. 2012, Science, 337, 1638
Lamy, P., Prado, J.-Y., Floyd, O., et al. 2015, Sol. Phys., 290, 2617
Mamajek, E. E., Prsa, A., Torres, G., et al. 2015, arXiv e-prints, arXiv:1510.07674
Mazarico, E., Rowlands, D. D., Neumann, G. A., et al. 2012, Journal of Geodesy, 86, 193
Meftah, M., Hauchecorne, A., Bush, R. I., & Irbah, A. 2016, Advances in Space Research, 58, 1425
Meftah, M., Corbard, T., Hauchecorne, A., et al. 2018, A&A, 616, A64
Neumann, G., Smith, D., Scott, S., Slavney, S., & Grayzek, E. 2011, National Aeronautics and Space Administration Planetary Data System: http://pds-geosciences.wustl.edu/missions/lro/lola.htm (accessed 20 August 2015)
Prša, A., Harmanec, P., Torres, G., et al. 2016, AJ, 152, 41
Rambaux, N., Castillo-Rogez, J. C., Williams, J. G., & Karatekin, Ö. 2010, Geophys. Res. Lett., 37, L04202
Raponi, A., Sigismondi, C., Guhl, K., Nugent, R., & Tegtmeier, A. 2012, Sol. Phys., 278, 269
Rozelot, J. P. 2006, Advances in Space Research, 37, 1649
Rozelot, J. P., & Damiani, C. 2011, European Physical Journal H, 36, 407
Rozelot, J. P., & Damiani, C. 2012, European Physical Journal H, 37, 709
Rozelot, J.-P., Kosovichev, A., & Kilcik, A. 2016, in Solar and Stellar Flares and their Effects on Planets, eds. A. G. Kosovichev, S. L. Hawley, & P. Heinzel, 320, 342
Rozelot, J. P., Kosovichev, A. G., & Kilcik, A. 2018a, A Brief History of the Solar Diameter Measurements: a Critical Quality Assessment of the Existing Data, eds. J. P. Rozelot & E. S. Babayev, Variability of the Sun and Sun-Like Stars: from Asteroseismology to Space Weather, 89 (arXiv:1609.02710)
Rozelot, J. P., Kosovichev, A. G., & Kilcik, A. 2018b, Sun and Geosphere, 13, 63 (arXiv:1804.06930)
Sigismondi, C., Raponi, A., Bazin, C., & Nugent, R. 2012, in International Journal of Modern Physics Conference Series, 12, 405
Smith, D. E., Zuber, M. T., Neumann, G. A., et al. 2010, Geophys. Res. Lett., 37, L18204
Sofia, S., Girard, T. M., Sofia, U. J., et al. 2013, MNRAS, 436, 2151
Soma, M., & Kato, Y. 2002, Publications of the National Astronomical Observatory of Japan, 6, 75
Thuillier, G., Sofia, S., & Haberreiter, M. 2005, Advances in Space Research, 35, 329
Tooley, C. R., Houghton, M. B., Saylor, R. S., et al. 2010, Space Sci. Rev., 150, 23
Urban, S. E., & Kenneth Seidelmann, P. 2013, Explanatory supplement to the astronomical almanac (University Science Books)
Watts, C. B. 1963, The marginal zone of the Moon, 17 (US Government Printing Office)
Wessel, P., Smith, W. H. F., Scharroo, R., Luis, J., & Wobbe, F. 2013, EOS Transactions, 94, 409
Williams, J., Boggs, D., & Folkner, W. 2013, DE430 Lunar Orbit, Physical Librations and Surface Coordinates, JPL Interoffice Memorandum (Internal Document), Jet Propulsion Laboratory, California Institute of Technology, Pasadena, California, 19
Yang, Y.-Z., Li, J.-L., Ping, J.-S., & Hanada, H. 2017, RAA (Research in Astronomy and Astrophysics), 17, 127